Pattern evolution in bending dielectric-elastomeric bilayers[☆]

Yipin Su [a,b], Bin Wu [c], Weiqiu Chen [a], Michel Destrade [b,a,*]

[a] *Department of Engineering Mechanics, Zhejiang University, Hangzhou 310027, PR China*
[b] *School of Mathematics, Statistics and Applied Mathematics, NUI Galway, University Road, Galway, Ireland*
[c] *Department of Mechanical and Aerospace Engineering, Politecnico di Torino, Torino 10129, Italy*

ABSTRACT

We propose theoretical and numerical analyses of smart bending deformation of a dielectric-elastic bilayer in response to a voltage, based on the nonlinear theory of electro-elasticity and the associated linearized incremental field theory. We reveal that the mechanism allowing the bending angle of the bilayer can be tuned by adjusting the applied voltage. Furthermore, we investigate how much the bilayer can be bent before it loses its stability by buckling when one of its faces is under too much compression. We find that the physical properties of the two layers must be selected to be of the same order of magnitude to obtain a consequent bending without encountering buckling. If required, the wrinkles can be designed to appear on either the inner or the outer bent surface of the buckled bilayer. We validate the results through comparison with those of the classical elastic problem.

© 2019 Elsevier Ltd. All rights reserved.

1. Introduction

Finite bending is a most common deformation of solids in nature and in engineering applications, generally triggered by the application of mechanical loads. We call this scenario, *mechanical bending*. In contrast, we use the denomination *smart bending* to refer to the bending deformation of solids that is intentionally activated by other controllable stimuli such as pH, temperature, electric field, magnetic field or light signals. Smart bending provides an effective way to realize intelligent control and has potential applications in actuators, soft robots, flexible electronics, bionic engineering, etc. Various controllable motions such as large-strain bending, helical curling, climbing, and even bionic actuations (wormlike self-walking motion and imitating human-hand actions) have been brought into life recently by smart bending, see examples in Fig. 1. On the other hand, little attention has been devoted to the theoretical investigation of the smart bending deformation of solids, and the physical mechanisms at play to achieve large and stable smart bending deformations of intelligent structures are still not completely understood.

A clever strategy to realize smart bending of a solid is to rely on a layered structure which generates bending moments due to the spatially differential stresses along its thickness induced by external stimuli (He et al., 2017; Morimoto and Ashida, 2015; Nardinocchi and Puntel, 2017). Motivated by the explosion of applications of dielectric elastomers – smart soft materials capable of large actuation deformation in fast response to electrical simulation – in actuators, soft robots
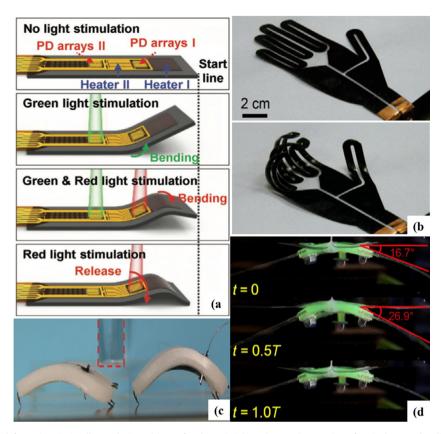

Fig. 1. Smart bending deformations in intelligent devices: (a) A soft robot mimicking the crawling motion of an inchworm: bending deformations occur in response to the alternating green and red laser lights and result in locomotion of the bimorph (Wang et al., 2018); (b) Bending deformation of a hand-shaped actuator, where the bending angle of each finger can be tuned by the applied voltage (Li et al., 2015); (c) A dielectric elastomer actuated soft robot can sneak under a barrier (red dashed line): here the wormlike self-walking motion is induced by tuning the voltage-induced bending angle of the elastomer (Li et al., 2018); (d) A self-powered soft robot made of dielectric elastomer and ionically conductive hydrogel mimics a swimming fish by periodically bending its fins (Li et al., 2017). (For interpretation of the references to color in this figure legend, the reader is referred to the web version of this article.)

and bioengineering (Brochu and Pei, 2010; O'Halloran et al., 2008; Pelrine et al., 2000), the aim of this work is to design a dielectric-elastomeric bilayer able to undergo large voltage-induced smart bending, and to reveal the physical mechanisms enabling a considerable finite bending deformation of the structure.

In this paper, we first propose a theoretical analysis of finite smart bending deformation of a dielectric-elastic bilayer in response to an applied voltage. The main idea is that by controlling the applied voltage, we control the extend of the bending deformation and thus achieve (theoretically) our goal of 'smart bending'. Here we adopt a nonlinear field theory (Dorfmann and Ogden, 2005; 2006; Suo et al., 2008) to describe the finite deformation coupled with an electric field, and find the optimal parameters for the bilayer to achieve a large bending angle.

Next, it is well known that theoretically, bending instability may occur in an extremely bent elastic solid (Destrade et al., 2009; Haughton, 1999). On the one hand, instability has long been recognized as a failure mode of structures and thus should be carefully analysed (Madsen et al., 2006). The onset of bending instability can be complicated by a layered structure, where many different routes can be taken to reach wrinkling, as shown by Bigoni and co-workers (Bigoni, 2012; Roccabianca et al., 2011; 2010). On the other hand, it was recently recognized that wrinkles could be beneficial and harvested to generate complex 3D architectures (Fu et al., 2018; Liu et al., 2016; Wu et al., 2013).

Here, we use the linearized incremental theory (Bertoldi and Gei, 2011; Bortot and Shmuel, 2018; Dorfmann and Ogden, 2010; Goshkoderia and Rudykh, 2017; Su et al., 2018) to further study the possible wrinkling of the bilayer caused by the large bending deformation.

The paper is structured as follows. In Section 2, we adopt the multiplicative decomposition method to derive the governing equations of the voltage-controlled bending deformation of dielectric-elastomeric bilayers. We then conduct a linearized stability analysis in Section 3 and use the surface impedance matrix method to predict the onset of wrinkles on the bent faces of the bilayer. The formulations developed in Sections 2 and 3 are valid for bilayers modeled by any form of energy function. In Section 4 we present numerical calculations for bilayers modelled with the Gent strain energy function (a model often used for strain-stiffening solids) to study the voltage-controlled bending deformation and its associated wrinkling

pattern evolution. We find that the physical parameters of the dielectric and elastic elastomers must be selected to be of the same order of magnitude to obtain a considerable bending angle. We also find that the wrinkles of an extremely bent bilayer can be intentionally designed to occur on either the inner or the outer bent face. Finally we draw some conclusions in Section 5.

2. Voltage-induced finite bending of a dielectric-elastomeric bilayer

Fig. 2 illustrates the mechanism at play in the dielectric-elastomeric bilayer and its bending. Consider two initially unde-formed incompressible elastomers, one dielectric and the other elastic, whose physical parameters are indicated henceforth with the superscripts 'd' and 'e', respectively. The initial thickness and length of the sth ($s = d, e$) block are H^s and L^s, re-spectively, μ^s denotes its initial mechanical shear modulus, and ε is the permittivity of the dielectric block.

Subject to a voltage V_1 along the thickness and a pre-stress P along the length, the dielectric block can be stretched to have the same length as the undeformed elastic block. Then the dielectric block is perfectly bonded to the elastic block along their length to form a bilayer (i.e., the stresses and displacements of the two elastomers are continuous at the interface). By releasing the pre-stress and reducing, in a controlled manner, the voltage to V_2 ($< V_1$), an inhomogeneous deformation takes place in the bilayer, which can result in a global bending, with bending angle φ, say.

In principle, we could induce the same mismatch by applying a pure mechanical pre-stress on the dielectric block, and a bending deformation of the bilayer would then result from releasing that stress. However, that pure mechanical bending deformation, in contrast to our smart bending deformation, is difficult to control in practice. Here we show that the voltage-induced bending deformation of the bilayer can be tuned effectively by varying the applied voltage only, which provides an effective way to realize intelligent control. Note that when the bilayer bends, the applied voltage is not completely off. Instead, it is reduced (eventually all the way to zero if desired) in a controlled way. We are thus solving an electromechanical coupling nonlinear problem, which has not been analyzed in literature before as far as we know.

The in-plane width of each block $A^d = A^e = A$ is taken to be much longer than its thickness and length, and so we make the *plane strain* deformation assumption to simplify the mathematical modeling (He et al., 2017; Morimoto and Ashida, 2015). We also assume that the materials are *incompressible*.

The total deformation gradient $\boldsymbol{F}^s$ of the bilayer, from the initial undeformed state to the current state of bending, is decomposed into two parts as shown in Fig. 2: $\boldsymbol{F}^s = \boldsymbol{F}_2^s \boldsymbol{F}_1^s$, where $\boldsymbol{F}_1^s$ is the (homogeneous) deformation gradient from the reference to the intermediate configuration, and $\boldsymbol{F}_2^s$ is the (inhomogeneous) deformation gradient of the deformation from the intermediate to the current configuration.
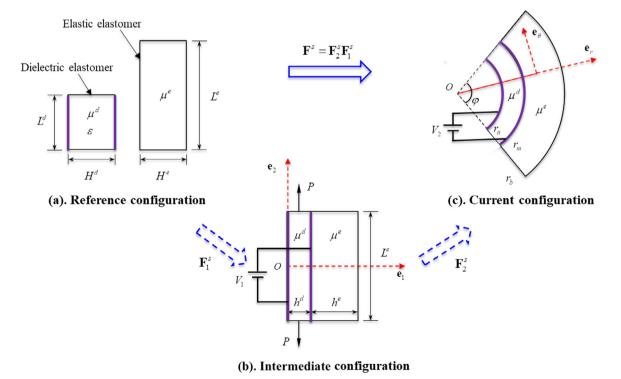

Fig. 2. Voltage-controlled bending deformation of a dielectric-elastic bilayer induced by inhomogeneous deformation and its multiplicative decomposition.

We first consider the homogeneous deformation of the layers from the reference configuration to the intermediate configuration, with the deformation gradients

$$\boldsymbol{F}_1^e = \boldsymbol{I}, \qquad \boldsymbol{F}_1^d = \text{diag}\big[(\lambda_1^d)^{-1}, \lambda_1^d, 1\big], \tag{1}$$

due to the plane strain assumption and the incompressibility of the materials. The deformed thicknesses and lengths are $h^e = H^e$, $h^d = (\lambda_1^d)^{-1}H^d$ and $l^e = l^d = L^e = \lambda_1^d L^d$, respectively.

Here, the stretch along the length of the dielectric block $\lambda_1^d = \lambda_1^d(V_1, P)$, subject to the combined action of voltage V_1 and pre-stress P, can be determined by solving the equation

$$\frac{\partial W_1^d}{\partial \lambda_1^d}(\lambda_1^d, D_1) = P, \tag{2}$$

where $W_1^d(\lambda_1^d, D_1)$ is the energy density of the dielectric elastomer and D_1 is the only non-zero component of the Lagrangian electric displacement along the thickness. It is connected with the applied voltage V_1 through

$$\frac{V_1}{H^d} = \frac{\partial W_1^d}{\partial D_1}(\lambda_1^d, D_1). \tag{3}$$

Following the homogeneous deformation $\boldsymbol{F}_1^s$, the bilayer occupies the region

$$0 \leq X_1 \leq h^d + h^e, \quad -L^e/2 \leq X_2 \leq L^e/2, \quad -A/2 \leq X_3 \leq A/2, \tag{4}$$

as depicted in Fig. 2.

We then consider the second (inhomogeneous) deformation stage from the intermediate to the current configuration. After releasing P and reducing V_1, the bilayer bends and occupies the current region

$$r_a \leq r \leq r_b, \quad -\varphi/2 \leq \theta \leq \varphi/2, \quad -A/2 \leq z \leq A/2, \tag{5}$$

by undergoing the following bending deformation (Green and Zerna, 1954; Ogden, 1997; Rivlin, 1949)

$$r = \sqrt{D + 2X_1/\omega}, \quad \theta = \omega X_2, \quad z = X_3. \tag{6}$$

Here (X_1, X_2, X_3) and (r, θ, z) are the rectangular Cartesian and cylindrical coordinates giving the position of an arbitrary point of the solid in the intermediate and current configurations, with orthogonal bases $(\boldsymbol{e}_1, \boldsymbol{e}_2, \boldsymbol{e}_3)$ and $(\boldsymbol{e}_r, \boldsymbol{e}_\theta, \boldsymbol{e}_z)$, respectively, and D and ω are constants to be determined. The inner, interfacial and outer radii and the bending angle of the deformed sector r_a, r_m, r_b and φ are given by

$$r_a = \sqrt{D}, \qquad r_m = \sqrt{D + \frac{2h^d}{\omega}}, \qquad r_b = \sqrt{D + \frac{2(h^d + h^e)}{\omega}}, \qquad \varphi = \omega L^e, \tag{7}$$

respectively. Note that the continuity of the displacement field is implicit in Eq. (7). Then the deformation gradient of the bilayer in this stage is

$$\boldsymbol{F}_2^s = \text{diag}\big[(\lambda_2^s)^{-1}, \lambda_2^s, 1\big], \tag{8}$$

in the $\boldsymbol{e}_i \otimes \boldsymbol{e}_j$ ($i = r, \theta, z$, $j = 1, 2, 3$) basis, where $\lambda_2^s = \omega r$ is the circumferential stretch of the solid in the current configuration.

Consequently, from Eqs. (1) and (8) the total deformation gradient of the bilayer from the reference configuration to the current configuration reads

$$\boldsymbol{F}^s = \boldsymbol{F}_2^s \boldsymbol{F}_1^s = \text{diag}\big[(\lambda^s)^{-1}, \lambda^s, 1\big], \tag{9}$$

where $\lambda^s = \lambda_1^s \omega r$ is the total circumferential stretch of the sth block; here $\lambda^d = \lambda_1^d \omega r$ and $\lambda^e = \omega r$.

From Eqs. (7)–(9) we derive the relationships

$$\lambda_m^d = \lambda_1^d \lambda_m^e, \qquad \frac{(\lambda_m^e)^2 - (\lambda_a/\lambda_1^d)^2}{(\lambda_b)^2 - (\lambda_a/\lambda_1^d)^2} = \frac{1}{1 + \lambda_1^d \overline{H}}, \tag{10}$$

where $\overline{H} = H^e/H^d$ is the ratio of the thicknesses of the elastic and dielectric elastomers, $\lambda_a = \lambda_1^d \omega r_a$, $\lambda_b = \omega r_b$ are the inner and outer circumferential stretches of the solid, and $\lambda_m^d = \lambda_1^d \omega r_m$, $\lambda_m^e = \omega r_m$ are the circumferential stretches of the dielectric and elastic elastomers at the interface, respectively. Note that the circumferential stretches of the two elastomers at the interface, λ_m^d and λ_m^e, are not the same.

According the theory of nonlinear electro-elasticity, the stresses in the radial and hoop directions of the solid are obtained as (Su et al., 2019b)

$$\tau_{rr}^d = W^d(\lambda^d, D_2) - W^d(\lambda_a, D_2), \quad \tau_{\theta\theta}^d = \lambda^d \frac{\partial W^d}{\partial \lambda^d}(\lambda^d, D_2) + W^d(\lambda^d, D_2) - W^d(\lambda_a, D_2),$$

$$\tau_{rr}^e = W^e(\lambda^e) - W^e(\lambda_b), \qquad\qquad \tau_{\theta\theta}^e = \lambda^e \frac{\partial W^e}{\partial \lambda^e}(\lambda^e) + W^e(\lambda^e) - W^e(\lambda_b), \tag{11}$$

where $W^d(\lambda^d, D_2)$ and $W^e(\lambda^e)$ are the energy densities of the dielectric and elastic elastomers, respectively, and D_2 is the only non-zero component of the Lagrangian electric displacement along the thickness associated with the applied voltage V_2. Note that we have used the equilibrium equation in the radial direction, and the traction-free conditions $\tau_{rr}^d(r_a) = \tau_{rr}^e(r_b) = 0$ at the inner and outer surfaces $r = r_a, r_b$ of the bilayer to derive Eq. (11).

The continuity of the radial stress field at the bonded interface between the dielectric and elastic blocks reads

$$\tau_{rr}^d(r_m) = \tau_{rr}^e(r_m). \tag{12}$$

Since there is no mechanical moment applied on the lateral boundaries $\theta = \pm\varphi/2$ of the bilayer, we have

$$\int_{r_a}^{r_m} \tau_{\theta\theta}^d r\,dr + \int_{r_m}^{r_b} \tau_{\theta\theta}^e r\,dr = 0. \tag{13}$$

Further, we showed elsewhere (Su et al., 2019b) that no normal force is required on the end faces to effect the bending, so that

$$\int_{r_a}^{r_m} \tau_{\theta\theta}^d\,dr + \int_{r_m}^{r_b} \tau_{\theta\theta}^e\,dr = 0. \tag{14}$$

Finally, the voltage difference between the two faces of the deformed dielectric elastomer is obtained as (Su et al., 2019b; Wu et al., 2017)

$$V_2 = \int_{r_a}^{r_m} E_r\,dr = \int_{r_a}^{r_m} \lambda^d \frac{\partial W^d}{\partial D_2}\,dr, \tag{15}$$

where $E_r = \lambda^d \partial W^d/\partial D_2$ is the true radial electric field in the deformed dielectric layer.

Summing up, we can determine $\lambda_1^d, \lambda_a, \lambda_m^d, \lambda_m^e$ and λ_b by solving Eqs. (2), (3), (10)–(13) and (15), once the loadings P, V_1 and V_2 are prescribed. We then obtain the bending angle from Eq. (7)$_4$ and the stress distribution in the bilayer from Eq. (11).

3. Linearized stability analysis

We adopt the linearized incremental theory (Bertoldi and Gei, 2011; Bortot and Shmuel, 2018; Dorfmann and Ogden, 2010; Goshkoderia and Rudykh, 2017; Su et al., 2018) to model the onset of buckling of the deformed bilayer and focus on the case when the applied voltage is completely removed ($V_2 = 0$). Readers may refer to the paper by Su et al. (2019b) for a detailed derivation of the formulas for a single dielectric elastomer. Here we just give the general equations governing the deformation of a small-amplitude perturbation superposed on the deformed dielectric elastomer; the incremental equations for the elastic elastomer are found from those for the dielectric elastomer by making the electric field vanish. Thus we omit the superscript in the following for ease of reading; and we will revert to the superscript notation to describe the boundary conditions and the interfacial conditions.

3.1. Incremental deformation

Upon the deformed configuration, we superimpose a small incremental displacement $\boldsymbol{u}$ and a small incremental (true) electric displacement $\dot{\boldsymbol{D}}$. Here and in the following the incremental quantities are denoted by a dot.

The incremental motion of the dielectric block is governed by the incremental equations of equilibrium and of incompressibility, which read

$$\mathrm{div}\,\dot{\boldsymbol{T}} = \boldsymbol{0}, \quad \mathrm{div}\,\dot{\boldsymbol{D}} = 0, \quad \mathrm{curl}\,\dot{\boldsymbol{E}} = 0, \quad \mathrm{div}\,\boldsymbol{u} = 0. \tag{16}$$

Here $\dot{\boldsymbol{T}} = \mathcal{A}(\mathrm{grad}\,\boldsymbol{u}) + \boldsymbol{\Gamma}\dot{\boldsymbol{D}} + p(\mathrm{grad}\,\boldsymbol{u}) - \dot{p}\boldsymbol{I}$ and $\dot{\boldsymbol{E}} = \boldsymbol{\Gamma}^T(\mathrm{grad}\,\boldsymbol{u}) + \boldsymbol{K}\dot{\boldsymbol{D}}$ are the incremental forms of Cauchy stress and true electric field, respectively, where p is a Lagrange multiplier associated with the incompressibility constraint and the fourth-, third- and second-order tensors $\mathcal{A}$, $\boldsymbol{\Gamma}$ and $\boldsymbol{K}$ are the effective electro-elastic moduli.

According to Eq. (16)$_3$, we may introduce an incremental electric potential $\dot{\phi}$ to rewrite the incremental electric field as $\dot{\boldsymbol{E}} = -\mathrm{grad}\,\dot{\phi}$.

We assume that there is no incremental traction on the inner and outer surfaces of the bent bilayer. The applied voltage is taken to be a constant to yield the following boundary conditions

$$\dot{T}_{rr}^d(r_a) = \dot{T}_{r\theta}^d(r_a) = \dot{\phi}^d(r_a) = \dot{T}_{rr}^e(r_b) = \dot{T}_{r\theta}^e(r_b) = \dot{\phi}^d(r_m) = 0. \tag{17}$$

Finally, because the two blocks are perfectly bonded, we have

$$\dot{T}_{rr}^d(r_m) = \dot{T}_{rr}^e(r_m), \quad \dot{T}_{r\theta}^d(r_m) = \dot{T}_{r\theta}^e(r_m). \tag{18}$$

3.2. The surface impedance method

The solution for the linear equations of the incremental deformation may be assumed in the form (Su et al., 2016)

$$u_r = U_r(r)\cos(n\theta), \qquad u_\theta = U_\theta(r)\sin(n\theta), \qquad \dot\phi = \Phi(r)\cos(n\theta),$$
$$\dot T_{rr} = \Sigma_{rr}(r)\cos(n\theta), \qquad \dot T_{r\theta} = \Sigma_{r\theta}(r)\sin(n\theta), \qquad \dot D_r = \Delta_r(r)\cos(n\theta), \tag{19}$$

where U_r, U_θ, Φ, Σ_{rr}, $\Sigma_{r\theta}$ and Δ_r are scalar functions of r only, and n is the circumferential wave number. It can be determined from the incremental traction free boundary conditions on the end faces $\theta = \pm\varphi/2$ as $n = 2q\pi/\varphi$ (Destrade et al., 2009), where the positive integer q gives the number of circumferential wrinkles of the solid when buckling occurs.

Then the governing equations of the incremental motion can be recast in the form of a first-order differential system, as

$$\frac{d}{dr}\boldsymbol\eta(r) = \frac{1}{r}\boldsymbol G\boldsymbol\eta(r) = \frac{1}{r}\begin{bmatrix} \boldsymbol G_1 & \boldsymbol G_2 \\ \boldsymbol G_3 & \boldsymbol G_4 \end{bmatrix}\boldsymbol\eta(r), \tag{20}$$

where $\boldsymbol\eta(r) = \begin{bmatrix} U_r & U_\theta & r\Delta_r & r\Sigma_{rr} & r\Sigma_{r\theta} & \Phi \end{bmatrix}^T = \begin{bmatrix} \boldsymbol U & \boldsymbol S \end{bmatrix}^T$ is the Stroh vector (with $\boldsymbol U = \begin{bmatrix} U_r & U_\theta & r\Delta_r \end{bmatrix}^T$ and $\boldsymbol S = \begin{bmatrix} r\Sigma_{rr} & r\Sigma_{r\theta} & \Phi \end{bmatrix}^T$), $\boldsymbol G$ is the Stroh matrix, with four 3×3 sub-blocks $\boldsymbol G_1$, $\boldsymbol G_2$, $\boldsymbol G_3$ and $\boldsymbol G_4$, given by

$$\boldsymbol G_1 = \begin{bmatrix} -1 & -n & 0 \\ \frac{n(\gamma_{12}-\tau_{rr})}{\gamma_{12}} & \frac{\gamma_{12}-\tau_{rr}}{\gamma_{12}} & 0 \\ -\frac{n^2\tau_{rr}}{\gamma_{12}}\frac{\Gamma_{122}}{K_{22}} & -\frac{n\tau_{rr}}{\gamma_{12}}\frac{\Gamma_{122}}{K_{22}} & 0 \end{bmatrix}, \quad \boldsymbol G_2 = \begin{bmatrix} 0 & 0 & 0 \\ 0 & \frac{1}{\gamma_{12}} & -\frac{n}{\gamma_{12}}\frac{\Gamma_{122}}{K_{22}} \\ 0 & \frac{n}{\gamma_{12}}\frac{\Gamma_{122}}{K_{022}} & -\frac{n^2}{K_{22}}\left(1+\frac{\Gamma_{122}^2}{K_{22}}\frac{1}{\gamma_{12}}\right) \end{bmatrix},$$

$$\boldsymbol G_3 = \begin{bmatrix} \kappa_{11} & \kappa_{12} & -(\Gamma_{111}-\Gamma_{221}) \\ \kappa_{12} & \kappa_{22} & -n(\Gamma_{111}-\Gamma_{221}) \\ \Gamma_{111}-\Gamma_{221} & n(\Gamma_{111}-\Gamma_{221}) & -K_{11} \end{bmatrix},$$

$$\boldsymbol G_4 = \begin{bmatrix} 1 & -\frac{n(\gamma_{12}-\tau_{rr})}{\gamma_{12}} & -\frac{n^2\tau_{rr}}{\gamma_{12}}\frac{\Gamma_{122}}{K_{22}} \\ n & -\frac{\gamma_{12}-\tau_{rr}}{\gamma_{12}} & -\frac{n\tau_{rr}}{\gamma_{12}}\frac{\Gamma_{122}}{K_{22}} \\ 0 & 0 & 0 \end{bmatrix}. \tag{21}$$

Here, we have

$$\gamma_{12} = \mathcal{A}_{1212} - \frac{\Gamma_{122}^2}{K_{22}}, \quad \gamma_{21} = \mathcal{A}_{2121} - \frac{\Gamma_{122}^2}{K_{22}},$$

$$\beta_{12} = \frac{1}{2}\left(\mathcal{A}_{1111} + \mathcal{A}_{2222} - 2\mathcal{A}_{1122} - 2\mathcal{A}_{1221} + \frac{2\Gamma_{122}^2}{K_{22}}\right),$$

$$\kappa_{11} = 2(\gamma_{12} - \tau_{rr} + \beta_{12}) + n^2\left[\gamma_{21} - \frac{(\gamma_{12}-\tau_{rr})^2}{\gamma_{12}}\right],$$

$$\kappa_{12} = n\left(\gamma_{12} + \gamma_{21} + 2\beta_{12} - \frac{\tau_{rr}^2}{\gamma_{12}}\right),$$

$$\kappa_{22} = 2n^2(\gamma_{12} - \tau_{rr} + \beta_{12}) + \gamma_{21} - \frac{(\gamma_{12}-\tau_{rr})^2}{\gamma_{12}}. \tag{22}$$

Note that by setting the voltage appearing in the Stroh matrix for the dielectric elastomer to be zero, we recover the Stroh matrix for the purely elastic elastomer.

Now the incremental boundary conditions (17) read

$$\boldsymbol S^d(r_a) = \boldsymbol S^e(r_b) = \boldsymbol 0, \tag{23}$$

and the incremental interfacial conditions (18) read

$$\boldsymbol S^d(r_m) = \boldsymbol S^e(r_m), \quad \boldsymbol U^d(r_m) = \boldsymbol U^e(r_m). \tag{24}$$

Define a conditional impedance matrix $\boldsymbol z^s(r, r_a)$ such that

$$\boldsymbol S^s(r) = \boldsymbol z^s(r, r_a)\boldsymbol U^s(r), \tag{25}$$

Then we use the surface impedance matrix method (Destrade et al., 2009; Du et al., 2018) to rewrite the Stroh differential system (20) as

$$\frac{d}{dr}\boldsymbol U^s = \frac{1}{r}\boldsymbol G_1^s\boldsymbol U^s + \frac{1}{r}\boldsymbol G_2^s\boldsymbol z^s\boldsymbol U^s, \quad \frac{d}{dr}(\boldsymbol z^s\boldsymbol U^s) = \frac{1}{r}\boldsymbol G_3^s\boldsymbol U^s + \frac{1}{r}\boldsymbol G_4^s\boldsymbol z^s\boldsymbol U^s. \tag{26}$$

The following Riccati differential equation can be obtained by elimination of $\boldsymbol{U}^s$ from Eq. (26)

$$\frac{d\boldsymbol{z}^s}{dr} = \frac{1}{r}(-\boldsymbol{z}^s\boldsymbol{G}_1^s - \boldsymbol{z}^s\boldsymbol{G}_2^s\boldsymbol{z}^s + \boldsymbol{G}_3^s + \boldsymbol{G}_4^s\boldsymbol{z}^s). \tag{27}$$

First we integrate Eq. (27) numerically for the dielectric layer, from r_a to r_m with the initial condition $\boldsymbol{z}^d(r_a, r_a) = \boldsymbol{0}$, to obtain $\boldsymbol{z}^d(r_m, r_a)$. Then we integrate Eq. (27) numerically for the elastic layer, from r_m to r_b with the initial condition $\boldsymbol{z}^e(r_m, r_a) = \boldsymbol{z}^d(r_m, r_a)$, to obtain $\boldsymbol{z}^e(r_b, r_a)$. Finally we tune the applied voltage V_1 until the following target condition is satisfied

$$\det \boldsymbol{z}^e(r_b, r_a) = 0, \tag{28}$$

which results from the boundary condition $\boldsymbol{S}^e(r_b) = \boldsymbol{0}$.

The conclusion is that for a dielectric-elastic bilayer with prescribed physical properties, the critical applied voltage V_{1c} of instability can be determined numerically, and so can the critical values of the bending angle φ_c and of the stretches λ_{1c}^d, λ_{ac}, λ_{mc}^d, λ_{mc}^e and λ_{bc}.

It follows from the condition $\boldsymbol{S}^e(r_b) = \boldsymbol{z}^e(r_b, r_a)\boldsymbol{U}^e(r_b) = \boldsymbol{0}$ that the ratios of the incremental motion on the outer face of the sector $t_\theta = U_\theta(r_b)/U_r(r_b)$, $t_\Phi = \Phi(r_b)/U_r(r_b)$ can be determined once $\boldsymbol{z}^e(r_b, r_a)$ is known. Now that the critical voltage V_{1c} has been obtained, we can define the other conditional impedance matrix $\boldsymbol{z}^s(r, r_b)$ in a similar way and integrate simultaneously the corresponding Eqs. (26) and (27) from r_b to r_a with the following initial conditions

$$\boldsymbol{U}(r_b) = U(r_b)\begin{bmatrix} 1 & t_\theta & t_\Phi \end{bmatrix}^{\mathrm{T}}, \quad \boldsymbol{z}^e(r_b, r_b) = \boldsymbol{0}, \tag{29}$$

where $U(r_b)$ is the arbitrary amplitude of the radial displacement on the outer surface. This integration determines the full distribution of the incremental field $\boldsymbol{U}^s(r)$ in the deformed sector and the corresponding buckling pattern.

4. Numerical results

4.1. Material model

Most polymers exhibit the strain stiffening effect, which can be well captured by the Gent model (Gent, 1996). In particular, the Gent model recovers the neo-Hookean model (Rivlin, 1948) as a limiting case, which describes solids with unlimited extensibility that do not exist in nature. See Fig. 3 for a comparison between the Gent and neo-Hookean responses.

For our calculations we use the ideal Gent dielectric model (Zhao and Suo, 2007) and the Gent elastic model to describe the dielectric and elastic elastomers, respectively, as

$$W_1^d(\lambda_1^d, D_1) = -\frac{\mu^d G^d}{2} \ln\left[1 - \frac{(\lambda_1^d)^2 + (\lambda_1^d)^{-2} - 2}{G^d}\right] + \frac{1}{2\varepsilon}(\lambda_1^d)^{-2}D_1^2,$$

$$W^d(\lambda^d, D_2) = -\frac{\mu^d G^d}{2} \ln\left[1 - \frac{(\lambda^d)^2 + (\lambda^d)^{-2} - 2}{G^d}\right] + \frac{1}{2\varepsilon}(\lambda^d)^{-2}D_2^2,$$
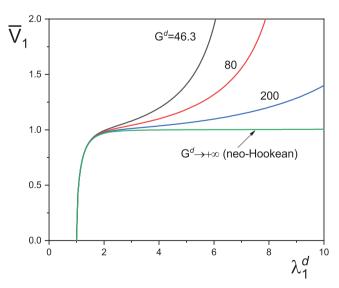

Fig. 3. Nonlinear behaviors of Gent dielectric elastomers for varying G^d subject to a voltage $\overline{V}_1$. The Gent model degenerates to the neo-Hookean model in the limiting case $G^d \to \infty$.

$$W^e(\lambda^e) = -\frac{\mu^e G^e}{2}\ln\left[1 - \frac{(\lambda^e)^2 + (\lambda^e)^{-2} - 2}{G^e}\right], \tag{30}$$

where G^s is the dimensionless stiffening parameter of the sth block. Throughout the paper, we use data as collected by Getz et al. (2017) for Silicone CF19-2186 from the manufacturer Nusil^{TM} (Nusil^{TM} Technology LLC, Carpinterio, USA) to model the dielectric elastomer, with $\mu^d = 333$kPa, $\varepsilon^d = 2.5 \times 10^{-11}$F/m, $G^d = 46.3$ and dielectric strength $E_B^d = 235$ MV/m. We set $G^e = 46.3$ for the elastic block also. Then the normalized breakdown electric field of the dielectric elastomer is $\overline{E}_B^d = E_B^d\sqrt{\varepsilon^d/\mu^d} = 2.04$. In the following calculations, the dimensionless actuation electric field of the dielectric elastomer is selected below this value to avoid electric breakdown failure.

From Eqs. (2) and (3), we determine the homogeneous stretch λ_1^d of the dielectric elastomer by solving the equation

$$\overline{P} = -\lambda_1^d\overline{V}_1^2 - \frac{G^d\left[(\lambda_1^d)^4 - 1\right]}{\lambda_1^d - (G^d + 2)(\lambda_1^d)^3 + (\lambda_1^d)^5}, \tag{31}$$

once the dimensionless pre-stress $\overline{P} = P/\mu$ and voltage $\overline{V}_1 = V_1\sqrt{\varepsilon/\mu^d}/H^d$ are prescribed. Since no mechanical loading is required to activate the bending deformation of the bilayer we have $\overline{P} = 0$ in the following calculations.

By solving Eq. (31) with $P = 0$, we obtain Fig. 3. It displays the nonlinear $\overline{V}_1 - \lambda_1^d$ response of the dielectric elastomer during the homogeneous deformation. The graph shows that the stretch λ_1^d increases monotonously with the increase of the applied voltage $\overline{V}_1$. Materials with finite G^d clearly exhibit the strain stiffening effect, and the stretchability of the material increases as G^d increases. Finally, note that the Gent model recovers the neo-Hookean model with infinite stretchability as $G^d \to \infty$. We note here that the *pull-in instability* can be avoided for dielectric elastomers under plane strain deformation, as shown by Yang et al. (2017) and Su et al. (2019a).

According to Eq. (11), we obtain the stresses in the radial and hoop directions of the bilayer as

$$\overline{\tau}_{rr}^d = \frac{G^d}{2}\ln\left[\frac{G^d - (\lambda_a)^{-2} - (\lambda_a)^2 + 2}{G^d - (\lambda^d)^{-2} - (\lambda^d)^2 + 2}\right] + \frac{\overline{D}_2^2}{2}\left[(\lambda^d)^{-2} - (\lambda_a)^{-2}\right],$$

$$\overline{\tau}_{rr}^e = \frac{G^e\overline{\mu}}{2}\ln\left[\frac{G^e - (\lambda_b)^{-2} - (\lambda_b)^2 + 2}{G^e - (\lambda^e)^{-2} - (\lambda^e)^2 + 2}\right],$$

$$\overline{\tau}_{\theta\theta}^d = \frac{G^d\left[(\lambda^d)^4 - 1\right]}{(2 + G^d)(\lambda^d)^2 - (\lambda^d)^4 - 1} + \frac{G^d}{2}\ln\left[\frac{G^d - (\lambda_a)^{-2} - (\lambda_a)^2 + 2}{G^d - (\lambda^d)^{-2} - (\lambda^d)^2 + 2}\right] - \frac{\overline{D}_2^2}{2}\left[(\lambda^d)^{-2} + (\lambda_a)^{-2}\right],$$

$$\overline{\tau}_{\theta\theta}^e = \frac{\overline{\mu}G^e\left[(\lambda^e)^4 - 1\right]}{(2 + G^e)(\lambda^e)^2 - (\lambda^e)^4 - 1} + \frac{\overline{\mu}G^e}{2}\ln\left[\frac{G^e - (\lambda_b)^{-2} - (\lambda_b)^2 + 2}{G^e - (\lambda^e)^{-2} - (\lambda^e)^2 + 2}\right]. \tag{32}$$

Then we determine D_2 with the connection (15) as

$$\overline{D}_2 = \frac{\overline{V}_2(\lambda_1^d)^2}{2}\left[(\lambda_m^e)^2 - \left(\frac{\lambda_a}{\lambda_1^d}\right)^2\right]\left(\ln\frac{\lambda_m^d}{\lambda_a}\right)^{-1}, \tag{33}$$
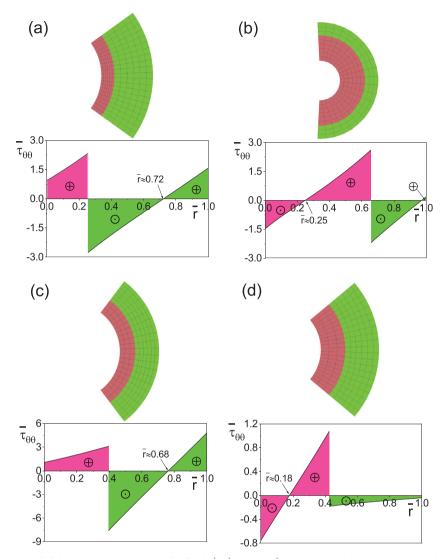
and the interfacial condition (12) reads

$$G^d\ln\left[\frac{G^d - (\lambda_a)^{-2} - (\lambda_a)^2 + 2}{G^d - (\lambda_m^d)^{-2} - (\lambda_m^d)^2 + 2}\right] + \overline{D}_2^2\left[(\lambda_m^d)^{-2} - (\lambda_a)^{-2}\right] = \overline{\mu}G^e\ln\left[\frac{G^e - (\lambda_b)^{-2} - (\lambda_b)^2 + 2}{G^e - (\lambda_m^e)^{-2} - (\lambda_m^e)^2 + 2}\right], \tag{34}$$

where $\overline{\tau}_{ii} = \tau_{ii}/\mu_d$ $(i = r, \theta)$, $\overline{V}_2 = V_2\sqrt{\varepsilon/\mu^d}/H^d$ and $\overline{D}_2 = D_2/\sqrt{\mu^d\varepsilon}$ are the dimensionless measures of τ_{ii}, V_2 and D_2, respectively, and $\overline{\mu} = \mu^e/\mu^d$ is the ratio of the shear moduli of the elastic and dielectric elastomers.

By using $\lambda^d = \lambda_1^d\omega r$ and $\lambda^e = \omega r$, Eq. (13) can be rewritten as

$$\left(\lambda_1^d\right)^{-2}\int_{\lambda_a}^{\lambda_m^d}\overline{\tau}_{\theta\theta}^d\lambda^d\,\mathrm{d}\lambda^d + \overline{\mu}\int_{\lambda_m^e}^{\lambda_b}\overline{\tau}_{\theta\theta}^e\lambda^e\,\mathrm{d}\lambda^e = 0. \tag{35}$$

The bending deformation of the bilayer can be completely determined by solving Eqs. (10) and (31)–(35), once the loadings $\overline{P}$, $\overline{V}_1$ and $\overline{V}_2$ are prescribed.

Fig. 4. Bending deformations of dielectric-elastomeric bilayers for fixed $L^d/H^d = 3$ and $G^d = G^e = 46.3$ and various thickness and shear modulus ratios in response to $\overline{V}_1 = 1, \overline{V}_2 = \overline{P} = 0$: (a) $\overline{H} = 2, \overline{\mu} = 2.5$; (b) $\overline{H} = 0.4, \overline{\mu} = 2.5$; (c) $\overline{H} = 1, \overline{\mu} = 10$; (d) $\overline{H} = 1, \overline{\mu} = 0.1$. The red and green phases represent the dielectric and elastic blocks, respectively. The top and bottom rows of each case correspond to the self-equilibrium shape and the associated hoop stress distribution of the bilayer, respectively. (For interpretation of the references to color in this figure legend, the reader is referred to the web version of this article.)

For the considered Gent elastomer with corresponding deformation gradient (9), we obtain the following components of the electro-elastic moduli tensors (with s omitted)
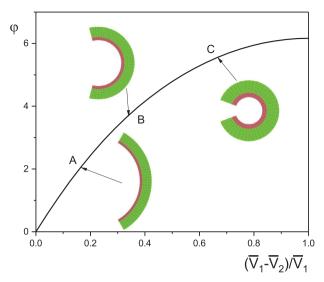
$$
\begin{aligned}
&\mathcal{A}_{1111} = \mu\big(2\lambda^{-2}\overline{W}_1 + 4\lambda^{-4}\overline{W}_{11} + \lambda^{-2}\overline{D}_2\big), && \mathcal{A}_{1122} = 4\mu\overline{W}_{11}, \\
&\mathcal{A}_{2222} = 2\mu\lambda^2(\overline{W}_1 + 2\lambda^2\overline{W}_{11}), && \mathcal{A}_{1221} = 0, \\
&\mathcal{A}_{1212} = \mu\lambda^{-2}(2\overline{W}_1 + \overline{D}_2^2), && \mathcal{A}_{2121} = 2\mu\lambda^2\overline{W}_1, \\
&\Gamma_{122} = \lambda^{-1}\overline{D}_2\sqrt{\mu\varepsilon^{-1}}, && K_{22} = \varepsilon^{-1},
\end{aligned}
\tag{36}
$$

where

$$
\overline{W}_1 = \frac{G\lambda^2}{2[(G+2)\lambda^2 - \lambda^4 - 1)]}, \qquad \overline{W}_{11} = \frac{G\lambda^4}{2[1 - (G+2)\lambda^2 + \lambda^4]^2}.
\tag{37}
$$

4.2. Bending response of the bilayer

In Fig. 4 we display the self-equilibrium shapes and the associated hoop stress distributions along the thickness of dielectric-elastomeric bilayers for various thickness and shear modulus ratios.

Fig. 5. Plot of bending angle φ as the function of voltage change $(\overline{V}_1 - \overline{V}_2)/\overline{V}_1$ for a dielectric-elastic bilayer with $L^d/H^d = 3$, $H^e/H^d = 1$, $\mu^e/\mu^d = 10$ and $G^d = G^e = 46.3$. The applied voltage to stretch the dielectric block is $\overline{V}_1 = 1.2$ and then is reduced gradually to zero. For the bilayers A, B and C, we have $\overline{V}_2 = 1$, 0.8 and 0.4, respectively.

We define $\bar{r} = (r - r_a)/(r_b - r_a)$ as the normalized radial position of a point in the bilayer. We first apply a constant voltage $\overline{V}_1 = 1$ to stretch the dielectric elastomer, and then take $\overline{V}_2 = 0$ to completely release it once the dielectric and elastic elastomers are perfectly bonded.

We can see that the physical parameters have significant influences on the bending response of the bilayer. The circumferential stresses of the two elastomers are discontinuous at the interface, which may result in slide, exfoliation or crack during the bending deformation of the bilayer thus should be avoided in film-substrate systems (Suo, 1995; Vella et al., 2009; Wang and Zhao, 2014). Both the dielectric and elastic elastomers can be finely designed to be transversely compressed or stretched, and the neutral axis which corresponds to vanishing circumferential stress can appear in the dielectric layer (case *d*), the elastic layer (cases *a, c*) or both the dielectric and elastic layers (case *b*). These results may provide guidance to design stretchable/flexible electronic devices where the active devices are placed on the neutral axis to avoid failure (Morimoto and Ashida, 2015).
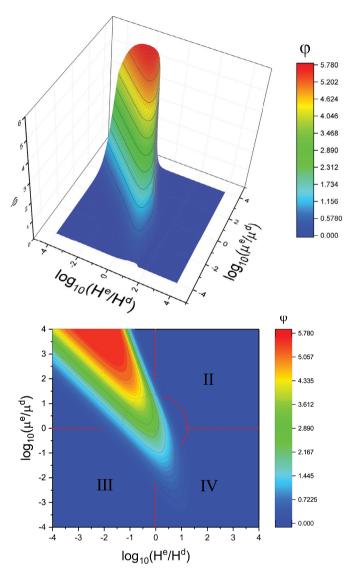
The effect of the applied voltage on the bending of the dielectric-elastic bilayer is presented in Fig. 5. We can see that the bending angle φ increases gradually as $(\overline{V}_1 - \overline{V}_2)/\overline{V}_1$ increases, i.e., the bilayer curls up as the applied voltage $\overline{V}_1$ reduces. In the calculation no mechanical loading is applied ($P = 0$), and we conclude that by solely tuning the applied voltage, the smart bending deformation of the bilayer can be designed to achieve desired motions, such as those presented in Fig. 1.

Fig. 6 displays the effects of the relative parameters of the two elastomers H^e/H^d and μ^d/μ^e on the bending angle φ of a bilayer with $L^d/H^d = 3$ and $G^d = G^e = 46.3$. We first apply a voltage $\overline{V}_1 = 0.8$ to stretch the dielectric block and then release the voltage once the two blocks are perfectly bonded ($\overline{V}_2 = 0$). It can be seen that the bending behavior of the bilayer is significantly influenced by the related parameters.

The physical mechanism behind the bending response of the bilayer can be understood as follows. If the dielectric block was by itself, it would shrink homogeneously in length to its initial configuration once the voltage $\overline{V}_1$ is released. The bonded elastic block prevents the recovery of the original dielectric block geometry, and results in an inhomogeneous deformation which triggers the bending deformation of the bilayer. If the constraint exerted by the elastic block on the deformation of the dielectric block is weak (e.g., the elastic block is thin and soft compared with the dielectric block as shown in Area III in Fig. 6), then the dielectric block deforms almost in its expected homogeneous way, and the bending of the bilayer can be almost ignored. On the other hand, if the elastic block is stiff and thick (Area II) or soft but extremely thick (Area IV), then the constraint exerted by the elastic block on the deformation of the dielectric block is so strong that the dielectric block almost keeps the same length as the elastic block, once they are bonded together. To achieve a large bending deformation, the shear modulus and the thickness of the dielectric phase of the bilayer should be of the same order of magnitude as those of the elastic phase (Area V), otherwise the dielectric phase of the bilayer should be soft but thick compared with the elastic phase (Area I).

4.3. Instability analysis

For the stability analysis, we focus on the scenario where the voltage is completely removed from the bilayer ($\overline{V}_2 = 0$), and find out how much it can be bent until wrinkles appear.

Fig. 6. Plot of bending angle φ as a function of $\log_{10}(H^e/H^d)$ and $\log_{10}(\mu^e/\mu^d)$ for a dielectric-elastic bilayer in the case where $L^d/H^d = 3$ and $G^d = G^m = 46.3$ (top) and its top view version (bottom). The applied voltage to initially stretch the dielectric block is $\overline{V}_1 = 0.8$ and then it is completely released ($\overline{V}_2 = 0$).

In Fig. 7 we compare the results of our model with those of the purely elastic problem. We take $G^d = G^e = 10^4$ to specialise the analysis to neo-Hookean materials (Destrade et al., 2009; Su et al., 2019b), and set $\overline{H} = \overline{\mu} = 1$.

Fig. 7 (a) displays the critical bending angle φ_c as a function of the aspect ratio of the dielectric elastomer L^d/H^d. By taking the number of wrinkles in turn as $q = 1, 2, 3, \ldots$ and solving the dispersive Eq. (28), we obtain a series of $\overline{V}_{1c} - L^d/H^d$ curves (in fact, they are each a scaled version of the $q = 1$ curve, see Destrade et al., 2009). Note that only the highest points located on the highlighted black bold curve are meaningful, as they indicate the earliest onset of instability. From this plot, the critical bending angle φ_c and the number of wrinkles q of the buckled bilayer can be predicted once L^d/H^d is given. We can see that the critical bending angle φ_c increases linearly as L^d/H^d increases, and that bilayers with $L^d/H^d > 3$ can be bent into closed tubes without buckling.

The variations of the associated critical stretches λ_{ac}, λ_{mc}^d, λ_{mc}^e and λ_{bc} with L^d/H^d are displayed in Fig. 7(a)–(e), respectively, with only the meaningful curves being presented. When $L^d/H^d \to 0$, the threshold of the bending instability approaches the critical stretch $\lambda_{ac} = 0.5437$ at which an incompressible neo-Hookean half-space under plane strain becomes unstable (Biot, 1963).

Results presented in Fig. 6 show that to obtain a considerable bending deformation, the properties of the bilayer should lie in Area I or Area V. We first consider bilayers from Area V. We can see from Fig. 8 that for these bilayers, the inner
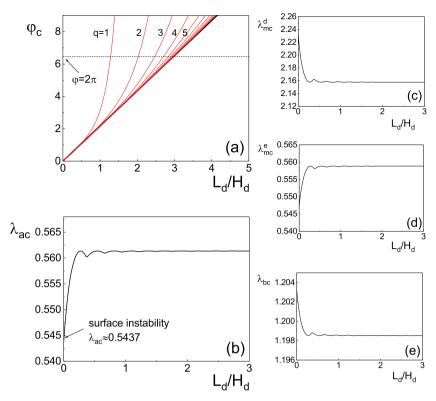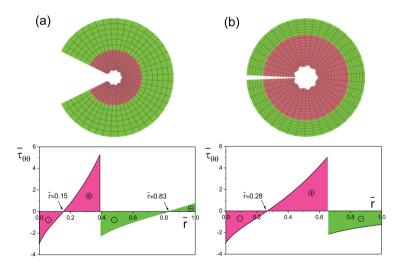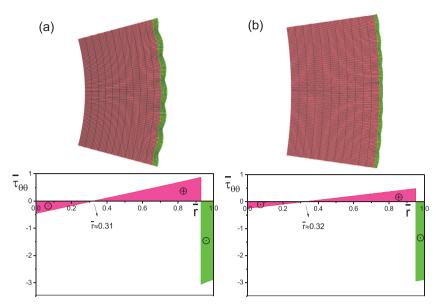
Fig. 7. Bending instability of a neo-Hookean ($G^d = G^e = 10^4$) dielectric-elastomeric bilayer with $\overline{H} = \overline{\mu} = 1$: the critical bending angle φ_c and the critical stretches λ_{ac}, λ_{mc}^d, λ_{mc}^e and λ_{bc} at the onset of buckling versus the width aspect ratio of the dielectric elastomer L^d/H^d are shown in (a)–(e), respectively.

Fig. 8. Bending instability of Gent dielectric-elastic bilayers with $G^d = G^e = 46.3$ and (a): $H^e/H^d = 1$, $\mu^e/\mu^d = 1$, $L^d/H^d = 3$ and (b): $H^e/H^d = 0.2$, $\mu^e/\mu^d = 0.5$, $L^d/H^d = 3$. The top row shows the wrinkling shapes when instability occurs, with 8 (Case (a)) and 9 (Case (b)) wrinkles occurring on the outer surface of the bilayer, as the applied voltage $\overline{V}_1$ reaches 1.17 and 1.38, respectively. The bottom row shows the distributions of the corresponding circumferential stresses in the bilayers.

part of the dielectric block is always compressed when buckling happens, and wrinkles appear on the inner surface of the dielectric block. The outer part of the elastic block can be either in tension (Fig. 8(a)) or in compression (Fig. 8(b)). The elastic elastomer is sufficiently soft and thick to sustain compression and wrinkles do not appear on its compressed face (when there is one). Notice that the perturbation decays rapidly along the radius, and that the displacement on the inner face is several orders of magnitude larger than that on the outer face. The material properties of the bilayer can be properly designed so that it can be bent into a closed tube ($\varphi_c > 2\pi$) without encountering buckling (not shown here).

Fig. 9. Elastic bending instability of a dielectric-elastic bilayer for fixed $G^d = G^e = 46.3$ and various phase properties: (a) $H^e/H^d = 0.05$, $\mu^e/\mu^d = 2.5$, $L^d/H^d = 2$; (b) $H^e/H^d = 0.03$, $\mu^e/\mu^d = 2.5$, $L^d/H^d = 2$. The top row shows the wrinkling shapes when instability occurs, with 6 and 9 wrinkles occur on the outer surface of the bilayer, as the applied voltages $\overline{V}_1$ reach 0.94 and 0.9, respectively. The bottom row shows the distributions of the corresponding circumferential stresses in the bilayers.

Next we consider instabilities of the bilayers from Area I, with results presented in Fig. 9. Here the elastic layer of the solid is always compressed, and because it is relatively stiff and thin compared with the dielectric layer, it cannot sustain compression and wrinkles appear. In this case, the bending deformation is relatively inconspicuous, and for the case $H^e/H^d \rightarrow 0$, the problem of instability of a layer resting on a substrate is recovered (Huang et al., 2005; Yin et al., 2018).

We observe that although theoretically the bilayers from Area I possess more favorable "bendability" than those from Area V, they are more susceptible to fail by the wrinkling instability.

5. Conclusion and discussion

In conclusion, we have investigated the bending response of a bilayer composed of a dielectric block and an elastic block in response to a voltage, and the associated buckling phenomenon, based on nonlinear theory of electro-elasticity and linearized incremental theory.

We first derived the governing equations of the static bending response of the bilayer for a general form of energy function, and obtained analytical solutions for Gent materials. We found that the bending angle of the bilayer can be tuned by the application of voltage and the relative physical parameters of the dielectric and elastic elastomers, and we revealed the mechanism required to obtain a considerable smart bending of the bilayer.

We recast the associated incremental problem in the form of first-order differential systems. We then used the surface impedance matrix method to build a robust numerical procedure for obtaining and solving the dispersion equation which predicts the critical condition when the bending instability occurs in the bilayer. We conducted calculations for Gent materials and recovered the results of the purely elastic problem. We showed that the pattern formation of a buckled bilayer can be selected by finely tuning the physical properties of the bilayer and the applied voltage.

The assumption of *plane strain deformation* was adopted to simplify the theoretical model of the problem by taking the in-plane width of each elastomer much longer than its thickness and length, but our analysis can easily be extended to the case of an arbitrary tri-axial pre-stretch (Haughton, 1999).

Viscoelasticity has been experimentally observed to have an effect on failure modes of dielectric elastomers (Plante and Dubowsky, 2006). To study its influence, a nonlinear field theory of viscoelastic electroelasticity (Hong, 2011) should be employed, which was beyond the scope of the current paper.

The results obtained here may provide references for the design and fabrication of dielectric-elastic bilayers that are capable of *finite smart bending*, and can be generalized to the case of smart bending activated by pH, temperature or light signals. They can also provide a basis for a *post-buckling analysis*, be it theoretical or numerical (Finite Element Method). As shown experimentally by Gent and Cho (1999), creases precede wrinkles on the inner face of bent rubber blocks. Indeed, a post-buckling analysis of compressed homogeneous half spaces reveals that creases are subcritical. However, when the half-space is coated with a layer of arbitrary thickness, creases can be supercritical when the layer is at least 1.74 times stiffer

than the substrate (Cai and Fu, 1999), in which case wrinkles do occur at the predicted linearised criterion and remain stable for a consequent compression (Cao and Hutchinson, 2012).

Acknowledgments

References

Bertoldi, K., Gei, M., 2011. Instabilities in multilayered soft dielectrics. J. Mech. Phys. Solids 59, 18–42.
Bigoni, D., 2012. Nonlinear Solid Mechanics: Bifurcation Theory and Material Instability. University Press, Cambridge.
Biot, M.A., 1963. Surface instability of rubber in compression. Appl. Sci. Res. A 12, 168–182.
Bortot, E., Shmuel, G., 2018. Prismatic bifurcations of soft dielectric tubes. Int. J. Eng. Sci. 124, 104–114.
Brochu, P., Pei, Q., 2010. Advances in dielectric elastomers for actuators and artificial muscles. Macromol. Rapid Comm. 31 (1), 10–36.
Cai, Z.X., Fu, Y.B., 1999. On the imperfection sensitivity of a coated elastic half-space. Proc. R. Soc. Lond. A 455, 3285–3309.
Cao, Y.P., Hutchinson, J.W., 2012. From wrinkles to creases in elastomers: the in-stability and imperfection-sensitivity of wrinkling. Proc. R. Soc. A 468, 94115.
Destrade, M., Ní Annaidh, A., Coman, C.D., 2009. Bending instabilities of soft biological tissues. Int. J. Solids Struct. 46 (25–26), 4322–4330.
Dorfmann, A., Ogden, R.W., 2005. Nonlinear electroelasticity. Acta Mech. 174 (3–4), 167–183.
Dorfmann, A., Ogden, R.W., 2006. Nonlinear electroelastic deformations. J. Elast. 82 (2), 99–127.
Dorfmann, A., Ogden, R.W., 2010. Nonlinear electroelastostatics: incremental equations and stability. Int. J. Eng. Sci. 48 (1), 1–14.
Du, Y.K., Lü, C.F., Chen, W.Q., Destrade, M., 2018. Modified multiplicative decomposition model for tissue growth: beyond the initial stress-free state. J. Mech. Phys. Solids 118, 133–151.
Fu, H.R., Nan, K.W., Bai, W.B., Huang, W., Bai, K., Lu, L.Y., Zhou, C.Q., Liu, Y.P., Liu, F., Wang, J.T., Han, M.D., Yan, Z., Luan, H.W., Zhang, Y.T., Zhao, J.N., Cheng, X., Li, M.Y., Lee, J.W., Liu, Y., Fang, D.N., Li, X.L., Huang, Y.G., Zhang, Y.H., Rogers, J., 2018. Morphable 3d mesostructures and microelectronic devices by multistable buckling mechanics. Nat. Mater. 17 (3), 268.
Gent, A.N., 1996. A new constitutive relation for rubber. Rubber Chem. Technol. 69 (1), 59–61.
Gent, A.N., Cho, I.S., 1999. Surface instabilities in compressed or bent rubber blocks. Rubber Chem. Technol. 72 (2), 253–262.
Getz, R., Kochmann, D.M., Shmuel, G., 2017. Voltage-controlled complete stopbands in two-dimensional soft dielectrics. Int. J. Solids Struct. 113, 24–36.
Goshkoderia, A., Rudykh, S., 2017. Electromechanical macroscopic instabilities in soft dielectric elastomer composites with periodic microstructures. Eur. J. Mech.-A/Solid. 65, 243–256.
Green, A.E., Zerna, W., 1954. Theoretical Elasticity. University Press, Oxford. Reprinted by Dover, New York.
Haughton, D.M., 1999. Flexure and compression of incompressible elastic plates. Int. J. Eng. Sci. 37, 16931708.
He, L.W., Lou, J., Du, J.K., Wang, J., 2017. Finite bending of a dielectric elastomer actuator and pre-stretch effects. Int. J. Mech. Sci. 122, 120–128.
Hong, W., 2011. Modeling viscoelastic dielectrics. J. Mech. Phys. Solids 59 (3), 637–650.
Huang, Z.Y., Hong, W., Suo, Z.G., 2005. Nonlinear analyses of wrinkles in a film bonded to a compliant substrate. J. Mech. Phys. Solids 53 (9), 2101–2118.
Li, Q.W., Liu, C.H., Lin, Y.H., Liu, L., Jiang, K.L., Fan, S.S., 2015. Large-strain, multiform movements from designable electrothermal actuators based on large highly anisotropic carbon nanotube sheets. ACS Nano 9 (1), 409–418.
Li, T.F., Li, G.R., Liang, Y.M., Cheng, T.Y., Dai, J., Yang, X.X., Liu, B.Y., Zeng, Z.D., Huang, Z.L., Luo, Y.W., Xie, T., Yang, W., 2017. Fast-moving soft electronic fish. Sci. Adv. 3 (4), e1602045.
Li, T.F., Zou, Z.N., Mao, G.Y., Yang, X.X., Liang, Y.M., Li, C., Qu, S.X., Yang, W., 2018. Agile and resilient insect-scale robot. soft robot.
Liu, Y., Yan, Z., Lin, Q., Guo, X.L., Han, M.D., Nan, K.W., Hwang, K.C., Huang, Y.G., Zhang, Y.H., Rogers, J.A., 2016. Guided formation of 3d helical mesostructures by mechanical buckling: analytical modeling and experimental validation. Adv. Funct. Mater. 26 (17), 2909–2918.
Madsen, H.O., Krenk, S., Lind, N.C., 2006. Methods of Structural Safety. Courier Corporation.
Morimoto, T., Ashida, F., 2015. Temperature-responsive bending of a bilayer gel. Int. J. Solids Struct. 56, 20–28.
Nardinocchi, P., Puntel, E., 2017. Swelling-induced wrinkling in layered gel beams. Proc. R. Soc. A 473 (2207), 20170454.
Ogden, R.W., 1997. Non-Linear Elastic Deformations. Dover, New York.
O'Halloran, A., O'Malley, F., McHugh, P., 2008. A review on dielectric elastomer actuators, technology, applications, and challenges. J. Appl. Phys. 104 (7), 9.
Pelrine, R., Kornbluh, R., Pei, Q., Joseph, J., 2000. High-speed electrically actuated elastomers with strain greater than 100%. Science 287 (5454), 836–839.
Plante, J.S., Dubowsky, S., 2006. Large-scale failure modes of dielectric elastomer actuators. Int. J. Solids Struct. 43 (25–26), 7727–7751.
Rivlin, R.S., 1948. Large elastic deformations of isotropic materials. i. fundamental concepts. Philos. Trans. R. Soc. Lond. 240 (822), 459–490.
Rivlin, R.S., 1949. Large elastic deformations of isotropic materials v: the problem of flexure. Proc. R. Soc. Lond. Ser. A 195, 463–473.
Roccabianca, S., Bigoni, D., Gei, M., 2011. Long wavelength bifurcations and multiple neutral axes of elastic layered structures subject to finite bending. J. Mech. Mater. Struct. 6 (1), 511–527.
Roccabianca, S., Gei, M., Bigoni, D., 2010. Plane strain bifurcations of elastic layered structures subject to finite bending: theory versus experiments. IMA J. Appl. Math. 75 (4), 525–548.
Su, Y.P., Broderick, H.C., Chen, W.Q., Destrade, M., 2018. Wrinkles in soft dielectric plates. J. Mech. Phys. Solids 119, 298–318.
Su, Y.P., Chen, W.Q., Destrade, M., 2019. Tuning the pull-in instability of soft dielectric elastomers through loading protocols. Int. J. Non-Lin. Mech. 113, 62–66.
Su, Y.P., Wu, B., Chen, W.Q., Destrade, M., 2019. Finite bending and pattern evolution of the associated instability for a dielectric elastomer slab. Int. J. Solids Struct. 158, 191–209.
Su, Y.P., Zhou, W.J., Chen, W.Q., Lü, C.F., 2016. On buckling of a soft incompressible electroactive hollow cylinder. Int. J. Solids Struct. 97–98, 400–416.
Suo, Z.G., 1995. Wrinkling of the oxide scale on an aluminum-containing alloy at high temperatures. J. Mech. Phys. Solids 43 (6), 829–846.
Suo, Z.G., Zhao, X.H., Greene, W.H., 2008. A nonlinear field theory of deformable dielectrics. J. Mech. Phys. Solids 56 (2), 467–486.
Vella, D., Bico, J., Boudaoud, A., Roman, B., Reis, P.M., 2009. The macroscopic delamination of thin films from elastic substrates. Proc. Natl. Acad. Sci. 106 (27), 10901–10906.
Wang, C.J., Sim, K., Chen, J., Kim, H.J., Rao, Z., Li, Y.H., Chen, W.Q., Song, J.Z., Verduzco, R., Yu, C.J., 2018. Soft ultrathin electronics innervated adaptive fully soft robots. Adv. Mater. 30 (13), 1706695.
Wang, Q.M., Zhao, X.H., 2014. Phase diagrams of instabilities in compressed film-substrate systems. J. Appl. Mech. 81 (5), 051004.

Wu, B., Su, Y.P., Chen, W.Q., Zhang, C.Z., 2017. On guided circumferential waves in soft electroactive tubes under radially inhomogeneous biasing fields. J. Mech. Phys. Solids 99, 116–145.

Wu, Z.L., Moshe, M., Greener, J., Therien-Aubin, H., Nie, Z., Sharon, E., Kumacheva, E., 2013. Three-dimensional shape transformations of hydrogel sheets induced by small-scale modulation of internal stresses. Nat. Commun. 4, 1586.

Yang, S.Y., Zhao, X.H., Sharma, P., 2017. Avoiding the pull-in instability of a dielectric elastomer film and the potential for increased actuation and energy harvesting. Soft Matter 13 (26), 4552–4558.

Yin, S.F., Li, B., Cao, Y.P., Feng, X.Q., 2018. Surface wrinkling of anisotropic films bonded on a compliant substrate. Int. J. Solids Struct. 141, 219–231.

Zhao, X.H., Suo, Z.G., 2007. Method to analyze electromechanical stability of dielectric elastomers. Appl. Phys. Lett. 91 (6), 061921.